Planetary and Space Science 58 (2010) 1475–1488

Contents lists available at ScienceDirect

Planetary and Space Science

journal homepage: www.elsevier.com/locate/pss

In-flight calibration of the Cassini imaging science sub-system cameras

Robert West [a,*], Benjamin Knowles [b], Emma Birath [b], Sebastien Charnoz [c], Daiana Di Nino [b], Matthew Hedman [d], Paul Helfenstein [e], Alfred McEwen [f], Jason Perry [f], Carolyn Porco [b], Julien Salmon [c], Henry Throop [g], Daren Wilson [b]

[a] Jet Propulsion Laboratory, California Institute of Technology, MS 169-237, 4800 Oak Grove Drive, Pasadena, CA 91109, USA
[b] CICLOPS/Space Science Institute, 4750 Walnut Street, Ste 205, Boulder, CO, USA
[c] UMR AIM, Université Paris Diderot/CEA/CNRS, CEA/SAp, Centre de l'Orme des Merisiers, 91191 Gif-Sur-Yvette, Cedex, France
[d] Department of Astronomy, Cornell University, Ithaca, NY 14853, USA
[e] CRSR, Cornell University, Ithaca, NY 14853, USA
[f] Lunar and Planetary Laboratory, University of Arizona, Tucson, AZ 85721, USA
[g] Southwest Research Institute, Boulder, CO 80302, USA

ARTICLE INFO

Article history:
Received 10 March 2010
Received in revised form
9 June 2010
Accepted 1 July 2010
Available online 23 July 2010

Keywords:
Instrumentation
Image processing
Photometry
Polarimetry
Experimental techniques

ABSTRACT

We describe in-flight calibration of the Cassini Imaging Science Sub-system narrow- and wide-angle cameras using data from 2004 to 2009. We report on the photometric performance of the cameras including the use of polarization filters, point spread functions over a dynamic range greater than 10^7, gain and loss of hot pixels, changes in flat fields, and an analysis of charge transfer efficiency. Hot pixel behavior is more complicated than can be understood by a process of activation by cosmic ray damage and deactivation by annealing. Point spread function (PSF) analysis revealed a ghost feature associated with the narrow-angle camera Green filter. More generally, the observed PSFs do not fall off with distance as rapidly as expected if diffraction were the primary contributor. Stray light produces significant signal far from the center of the PSF. Our photometric analysis made use of calibrated spectra from eighteen stars and the spectral shape of the satellite Enceladus. The analysis revealed a shutter offset that differed from pre-launch calibration. It affects the shortest exposures. Star photometry results are reproducible to a few percent in most filters. No degradation in charge transfer efficiency has been detected although uncertainties are large. The results of this work have been digitally archived and incorporated into our calibration software CISSCAL available online.

1. Introduction

The Cassini imaging science sub-system (ISS) consists of two cameras on the Cassini spacecraft. The cameras were built by the Jet Propulsion Laboratory, California Institute of Technology. The spacecraft was launched in October 1997, and has been in orbit around Saturn since July 2004. The scientific and technical background for the ISS instrument, and initial calibration tables, including final in-flight geometric calibrations were described by Porco et al. (2004). In this paper we focus on our in-flight experience with emphasis on target and data selection criteria and methods. We start by briefly describing the cameras (optics, detectors, shutter and filters). We then discuss methods and results for a variety of instrument in-flight calibrations. Results are presented in the context of our calibration software package named CISSCAL (Cassini ISS CALibration), which runs in the interactive data language (IDL) environment. The latest versions of the CISSCAL calibration volumes, including software, calibration files, sample calibration images and documentation, can be found on the CICLOPS website at http://ciclops.org/sci/cisscal.php and also at the Planetary Data System Imaging Node website at http://pds-imaging.jpl.nasa.gov/data/cassini/cassini_orbiter/coiss_0011_v2/extras/. All tables and digital files needed for the calibration (except point spread functions) are bundled with the software. In the future we plan to include the point spread functions.

2. Camera descriptions

Porco et al. (2004) provided comprehensive descriptions of the Cassini ISS narrow angle camera (NAC) and wide angle camera (WAC), including schematic diagrams of the structures and coordinate systems, filter characteristics, location of filters in the filter wheels, summation modes, image compression, coherent noise, and other attributes. Here we very briefly mention the

* Corresponding author. Tel.: +1 8183540479; fax: +1 8183934619.
E-mail address: Robert.A.West@jpl.nasa.gov (R. West).

0032-0633/$ - see front matter © 2010 Elsevier B.V.. All rights reserved.
doi:10.1016/j.pss.2010.07.006

key elements most relevant to in-flight calibration. Schematic views of the cameras appear in Figs. 1 and 2

The NAC is a reflector with a Ritchey–Chretien design to eliminate coma out to the edge of the field. This design improves image quality and simplifies image deconvolution since the point spread function (PSF) should be nearly independent of position. The WAC is a refractor, using spare optics (but new detector and filter wheel) from the Voyager mission. Both cameras use a 1024×1024-element charge-coupled device (CCD) array detector. Image scale is 5.9907 μr/pixel for the NAC and 59.749 μr/pixel for the WAC. Geometric distortion is small and is described by Porco et al. (2004). The cameras contain interference filters that were created by ion-aided deposition which produces a very stable product, immune to humidity and insensitive to temperature variations. Each camera contains two filter wheels which are used in tandem. Filter characteristics are listed in Tables VIII, IX XIV and XV of Porco et al. (2004), and transmission plots are shown in several figures of that paper. In addition polarizing filters can be paired with filters in the opposite wheel.

3. Residual bulk image and hot pixels

The cameras are framing devices with a mechanical shutter that controls exposure times. A radiative cooler combined with an electrical heater keep the detectors at a constant temperature (-90 °C). At that temperature a residual bulk image (hereafter RBI) leaks into the potential wells with a time constant comparable to an image readout time. This effect introduces a residual signal that depends on previous exposure to light. To establish a repeatable starting condition the detectors are flooded with light from lamps near the detector and then the CCD is clocked out to remove charge in the potential wells just before each exposure. We call this "pre-flash". Although the detector state is always initialized in the same way, charge from the pre-flash that leaks into potential wells during the exposure and during readout depends on exposure time and readout rate. Exposure times range from a few milliseconds to 1200 s and readout rates depend on many variables and can change during the readout. The resulting dark field is a spatially varying field that has a complicated dependence on many variables.

Dark frames were obtained for a range of exposure times from 0 to 1200 s by performing a normal exposure procedure but keeping the shutter closed. From these images we measure the rate of RBI leakage as a function of time. These images, like all the others, were first flooded by the pre-flash and then the CCD was read out before the exposure began. Understanding the dark field requires that the concept of "pixel" be refined to distinguish physical location on the chip, and the potential well associated with that physical location as a function of time. Once the readout starts the potential wells are clocked (shifted at the clocking rate) down the CCD until they reach the readout register and are then shifted out of the readout register. As they are clocked down they pick up charge from physical locations downstream of the originating physical location. Our initial thinking on how to model pre-flash RBI was outlined in Section 3.11 of Porco et al. (2004). Our implementation is a little different than the one described in that document. Instead of fitting a variety of dark

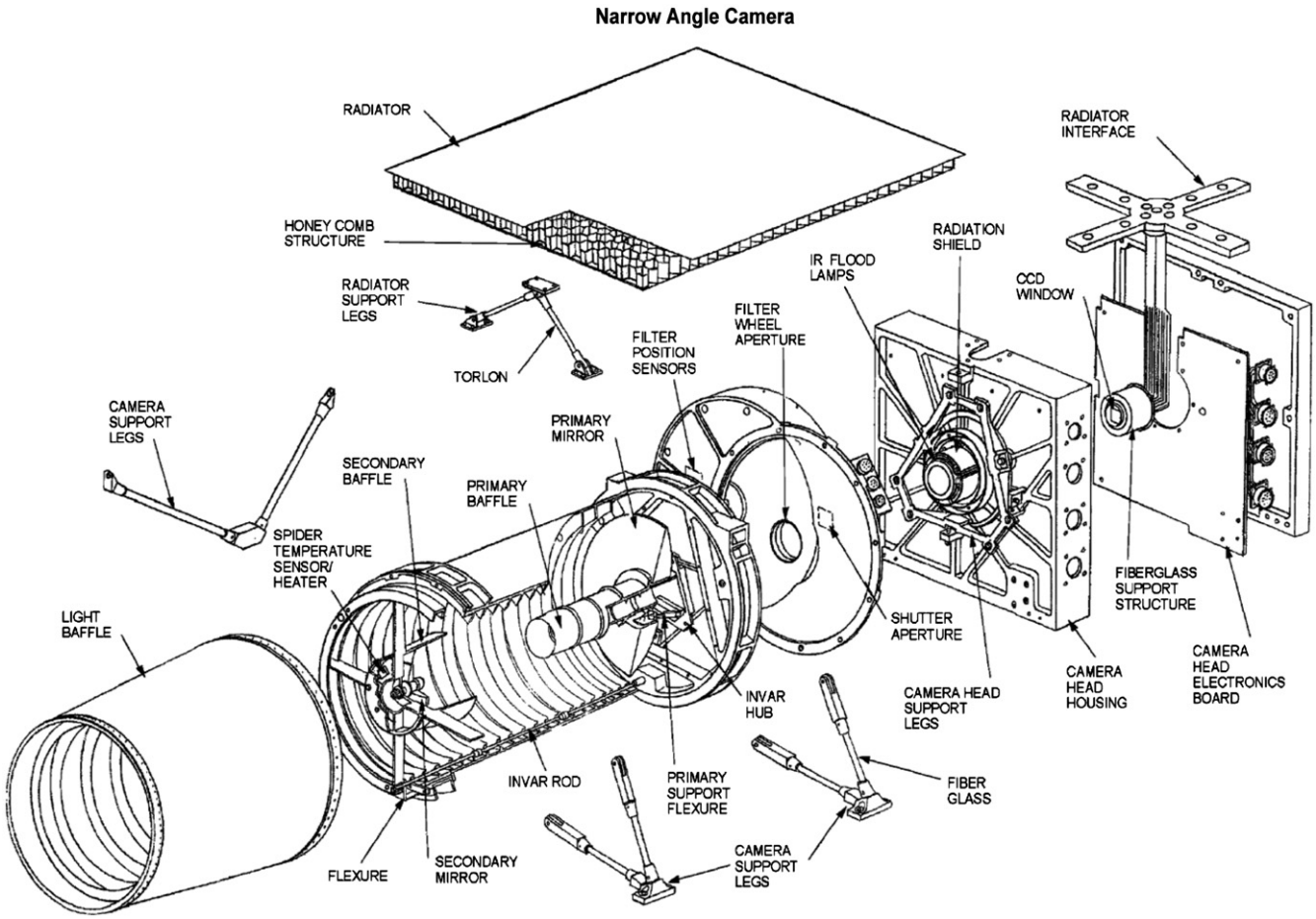

Fig. 1. This schematic diagram of the Cassini ISS narrow angle camera shows key optical, structural and sensor components. From Porco et al. (2004).

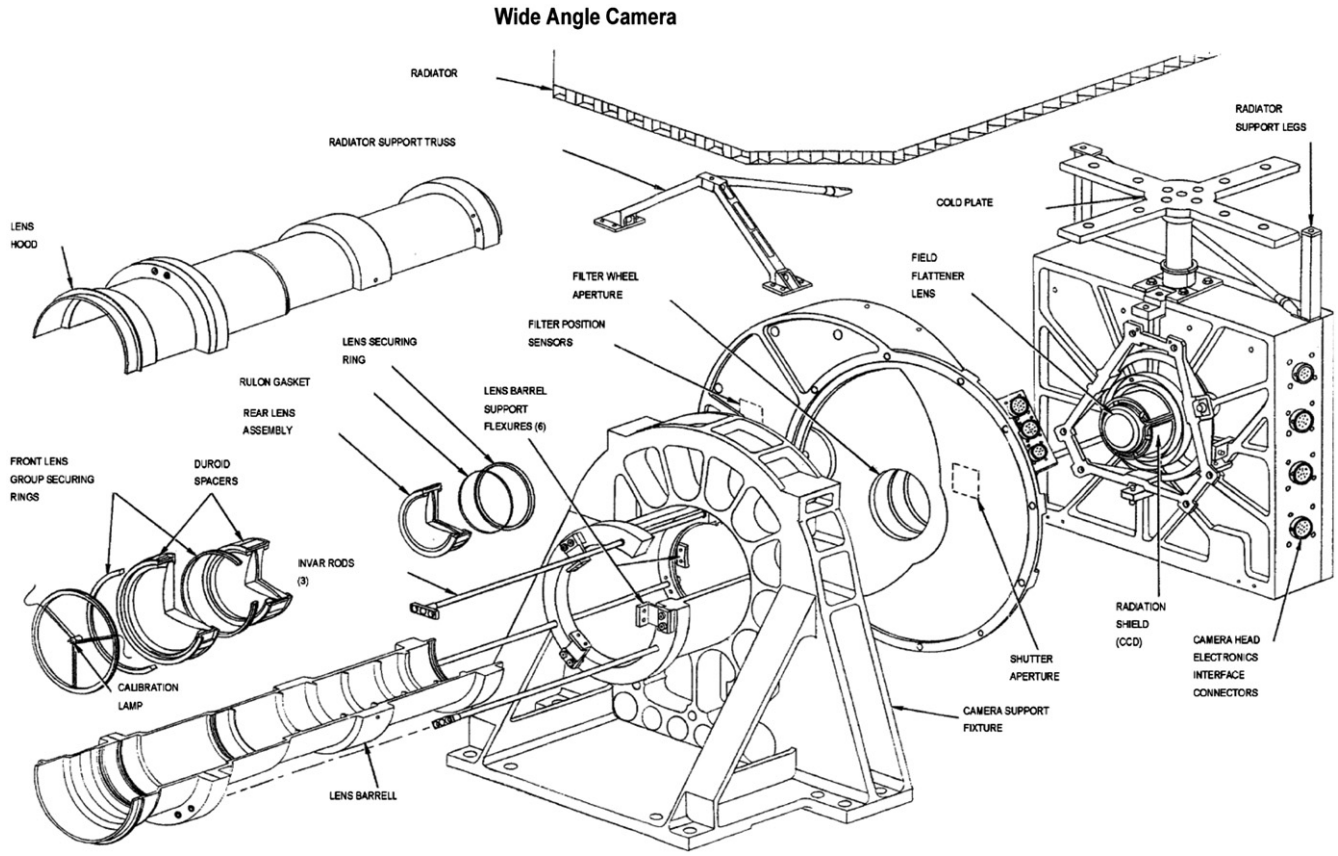

Fig. 2. The WAC optical, structural and sensor components. From Porco et al. (2004).

exposure values to coefficients of exponential sums we simply interpolate each pixel in the time domain. Derivation of the interpolation values requires an inversion code that accounts for accumulation of charge as each potential well moves over physical locations downstream of the originating location. The interpolation is much more stable and faster than the parameter fitting. The derived calibration values are the number of electrons emitted at each physical location as a function of time from the start of the exposure. These are stored in files and later read and interpolated to calculate output electrons for each physical location as a function of time. The calculated dark field for pixel $[i,j]$, where i is the sample number (horizontal coordinate in the image) and j is the line number (vertical coordinate), is then the sum of the contributions of the originating location and all locations downstream of $[i,j]$ as given by

$$D_{i,j} = \sum_{k=j,1} RBI(i,k,t_2) - RBI(i,k,t_1) \quad (1)$$

In Eq. (1) t_1 and t_2 are times when the potential well originating at physical location $[i,j]$ enters and leaves physical location $[i,k]$.

This calculation requires a computation of the dwell time for a potential well at its originating physical location and at each downstream location as the chip is read out. Since the RBI leakage rate decreases with elapsed time from the pre-flash, both the entry time (the time that a potential well begins to accumulate charge at a given physical location) and exit time must be computed. The timing is a complicated function of the telemetry rate, summation state (unsummed, 2×2 or 4×4), camera (NAC or WAC), compression (lossy or lossless, and lossy parameters) and image entropy (which depends on scene entropy, gain state and accumulated signal). For example, if the BOTSIM image mode is used (BOTh cameras SIMultaneous) the NAC and WAC both read to the buffer until the buffer fills. At that point the WAC stops reading out and only resumes when the buffer becomes available. The interaction with the buffer causes the last part of the image to read out more slowly than the first part and so the dark field is higher and has a different slope (signal as a function of line number) in the latter part of the image. The transition (line number) where this occurs depends on the other parameters mentioned above. Since there is a large number of possible combinations of parameters that affect the readout rate it is impractical to pre-compute dark images. Rather, they are created as needed and stored in a user archive on the user's computer. If additional images have the same set of parameters the relevant dark file can be retrieved from the archive more quickly than creating a new one. For this reason a special naming convention governs the archival dark files so that future dark calculations can test if the relevant file is available.

Some pixels (at locations of defects in the silicon caused by cosmic rays, gamma rays from the spacecraft radioactive thermal power generators, or from the manufacturing process) have an unusually high electron emission rate. These can also be treated with Eq. (1), but in this case it is not RBI but rather electron emission from defects. We call these "hot pixels". From cumulative energetic particle or gamma-ray damage we expect to see changes in the number and locations of these over time. We have examined the behavior of dark frames over the 4-year period from 2004 to 2008 and find that the RBI field has not changed but there are changes in the hot pixel field. These changes are now incorporated in a time-dependent dark field algorithm in CISSCAL. Table 1 lists the dates and number of pixels in the hot pixel list. Annealing of the silicon over time can repair defects and perhaps accounts for the observation than a few hot pixels return to

Table 1
Updates for NAC and WAC hot pixels.

Image ID range	Epoch	Number of hot pixels
I. *NAC hot pixels*		
N1461810061–N1461815946	2004.3	1548
N1474408984–N1471821728	2004.7	2066
N1482070223–N1482068963	2005.0	2171
N1515164115–N1515173591	2006.0	2452
N1544295065–N1544302693	2006.9	2580
N1579619227–N1579632401	2008.1	2852
N1591853188–N1591862664	2008.5	2944
II. *WAC hot pixels*		
W1461645122–W1461648643	2004.3	1292
W1474410099–W1471821728	2004.7	1980
W1482071734–W1482070474	2005.0	1949
W1512422616–W1512411194	2005.9	2145
W1514975604–W1514981960	2006.0	2197
W1528601516–W1528610114	2006.4	2256
W1544312473–W1544320101	2006.9	2337
W1578757861–W1578770861	2008.1	2571
W1591252254–W1591256170	2008.5	2542
W1610989968–W1611003390	2009.1	2596

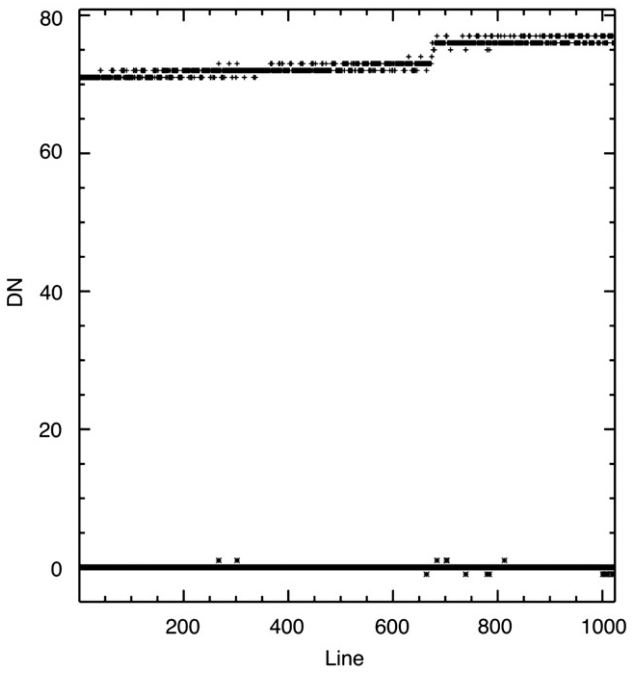

Fig. 3. Data number (DN) values for an eleven-pixel median average centered on sample 512 of each line of frame W1471313083 appear in the range 71–77 DN, increasing with line number and with a small discontinuity near line 660 caused by a "buffer full" pause. Points near the bottom of the figure (all but a few are zero) show the result of subtraction of dark image, bias subtraction (a constant value near 71 DN) and removal of 2-Hz noise which accounts for most of the variance in the raw values.

normal activity over time. The number of pixels identified as hot nearly doubled between 2004 and 2009, from 1548 to 2944 in the NAC and from 1292 to 2956 in the WAC.

An example of the dark subtraction is shown in Fig. 3. Residuals after dark subtraction and 2-Hz removal are less than 1 DN for most pixels provided the image is uncompressed or losslessly compressed and 12-bit encoded. Larger residuals, closer to 1 DN, are typical when 12-to-8 encoding is used due to higher quantization uncertainty. If there are gaps due to data losses the 2-Hz estimation produces larger errors (up to several DN) near the gaps. We expect that this could be improved with a better algorithm for 2-Hz removal.

4. Flat fields

Flat field refers to the relative (pixel-to-pixel) sensitivity of the detector. There is no calibration target on the Cassini spacecraft. To look for changes in the flat field we must rely on images of Venus or Titan which show very little contrast. The only changes that we are able to retrieve thus far are annular rings caused by dust specs on the optical components near the detector (the window on the detector package, or the quartz field flattener, for example). One new dust ring was noted in the Venus images early in the mission and has been part of the CISSCAL flat field ever since.

More recent changes were all detected at Titan close flybys. The assessment of changes in flat field is complicated by intensity gradients due to lighting and viewing geometry and by muted surface contrasts. However, dust rings have a characteristic annular shape that can be identified and not confused with background clutter. The ideal time to image Titan is when the spacecraft is close enough that Titan's angular diameter is much larger than the field of view of the camera and when the camera can point at a spot far from the terminator and limb where the intensity gradient is small. These are also the best times for a variety of instruments to take science data and due to the intense competition for pointing control and data volume we have not been able to obtain flat field images except in the NAC CB3 and MT1 filters which are heavily used for science. We plan to schedule future exposures to expand coverage and to sample as many WAC filters as the resources permit. The infrequent nature of the Titan passes and the requirement for low phase angle at close range for these measurements means that we have a measure of changes in the flat field at several widely spaced times during the mission, and it is not possible to know to a finer time sample when observed changes occurred.

Fig. 4 shows changes in the flat field (rings) due to the accumulation of dust on the optical components near the detector. The ring radius depends on the distance of the dust particle to the detector. Other features in the figure may or may not constitute changes in flat fields but some are due to differences in lighting conditions between the two time samples. We have also taken exposures with the calibration lamp on the WAC. Although the lamp is not imaged, the intensity field is highly structured across the detector. We see changes but the interpretation is not clear. They may be due to a small positional change in the lamp.

5. Charge transfer efficiency

The charge transfer efficiency (CTE) is a measure of how well electrons are transferred from one line to the next as the image is read off of the CCD. Ideally, CTE should be 1.0, meaning that none are trapped in the silicon. However, as damage from energetic particle and photon bombardment accumulates on the CCD the resulting defects (charge traps) can diminish the charge transfer efficiency, and this will have an impact on the ability to calibrate images. The energetic particle environment during cruise and in orbit about Saturn is considerably more benign than it is for the Hubble Space Telescope, which operates inside the Van Allen belts, and so degradation to the Cassini detectors is likely to be less severe than it was for the Wide Field and Planetary Camera 2 on the Hubble Space Telescope that used the same type of

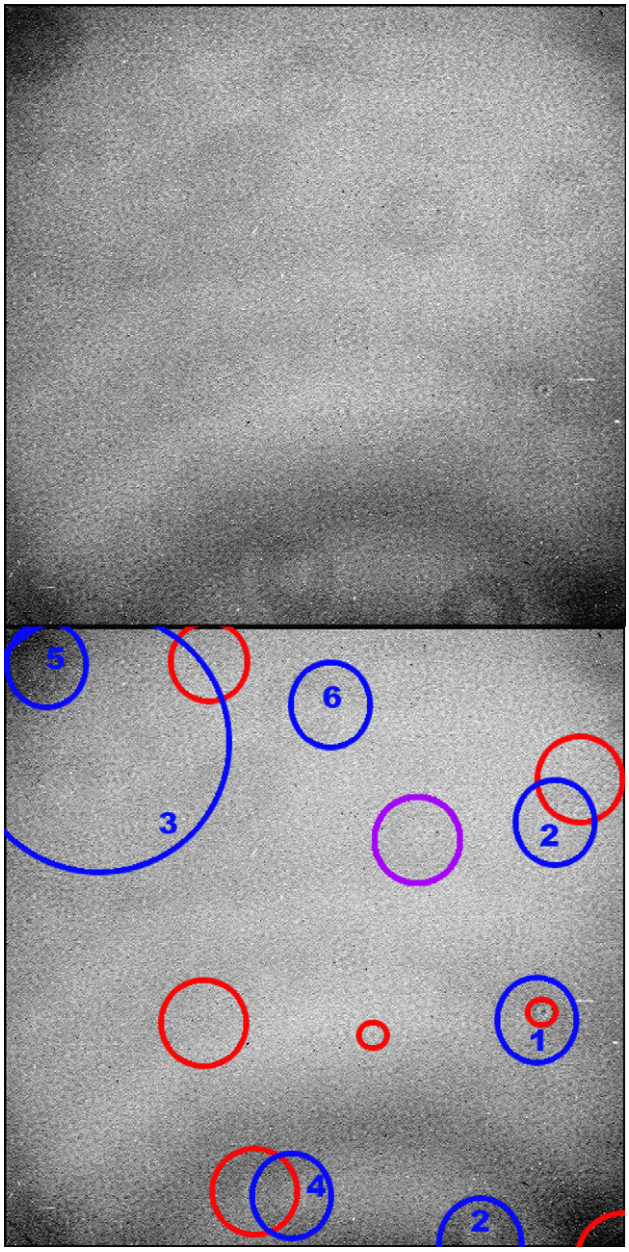

Fig. 4. The top panel shows new rings associated with dust on the optical components near the NAC detector, from a set of images in the CB3 filter. The contrast in the image is strongly amplified. The magnitude of these features is typically less than 1% although a few are stronger. The bottom panel identifies the features in terms of when they were found (see numbering scheme below). The unnumbered circled features point to features that were visible in data from the first two Titan flybys and are present to this day (or at least Rev 93 and Rev 110; Rev is the orbit number). The numbered circled features represent changes since flyby Tb (2004 day 346) and the number identifies the period in which they were found (see below). The purple circled feature was visible in images from flybys Ta and Tb as a "broken" annulus. By Rev 013, the annulus had filled out on its lower right side and had darkened. Below is a chronology of the tracked changes (epochs of differenced images): (1)Rev 013 and Rev 017 (2005-234 and 2005-302), (2) Rev 031 and Rev 038 (2006-298 and 2007-029) [2 changes], (3) Rev 049 and Rev 052 (2007-243 and 2007-323), (4) Rev 052 and Rev 053 (2007-323 and 2007-339), (5) Rev 055 and Rev 062 (2008-005 and 2008-085), (6) Rev 062 and Rev 093 (2008-085 and 2008-324).

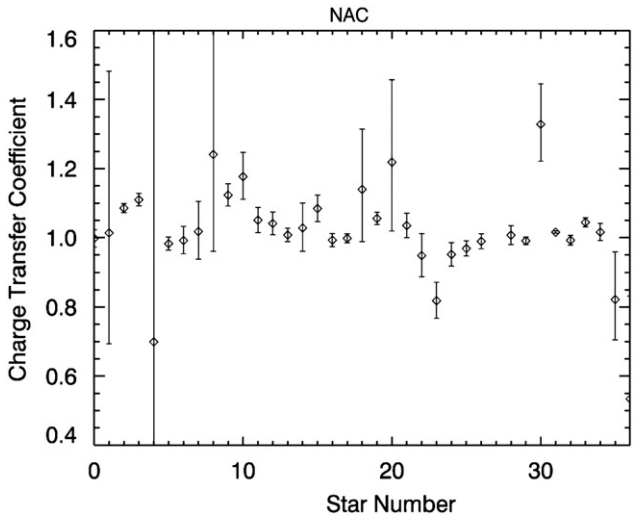

Fig. 5. Results of charge transfer efficiency analysis for the NAC computed by least-squares fits to apparent brightness as a function of line or sample number for 340 NAC images of 36 stars. The ordinate is labeled charge transfer coefficient rather than charge transfer efficiency to call attention to the fact that these are fitted coefficients.

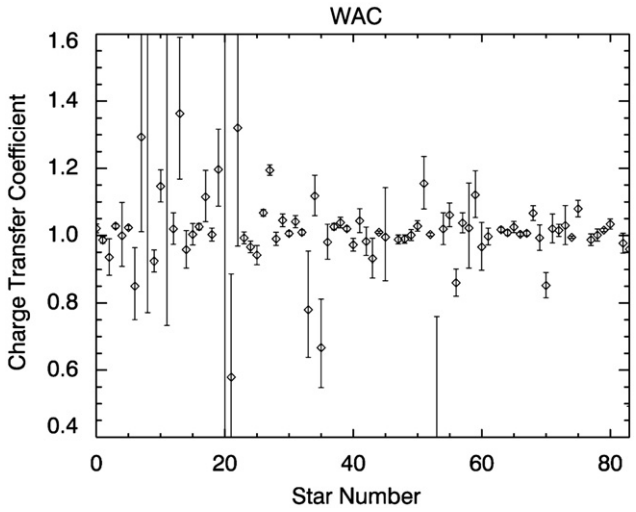

Fig. 6. Results of charge transfer efficiency analysis for the WAC for 86 stars on 49 images.

detectors. Charge transfer efficiency prior to launch was measured for the Cassini devices to be 0.99994. To measure charge transfer efficiency in flight we imaged star cluster M48 with the NAC and the Pleiades with the WAC. The intent was to image many stars at once, rotate the spacecraft by 30° about the optical axis and take another image, and repeat such that we could plot the charge as a function of line number and sample number. Fitting a straight line to the data plotted in that fashion would yield the charge transfer efficiency.

The results of such fits are shown in Figs. 5 and 6. The ordinate, labeled "charge transfer efficiency" is actually the CTE inferred from the difference in star flux divided by the difference in the number of line transfers from one image to the next as the spacecraft rotated. Some of the points on the plot are higher than 1.0. We do not believe the CTE is higher than 1.0. Rather, this plot shows that measurement error exceeds our ability to measure CTE with this method. The vertical bars indicate uncertainty for each star. The uncertainties are largest for faintest stars and for stars near the center of the image where image rotation produces only a small change in the vertical location of the star in the image. The resulting composite (fitted) uncertainty is 0.14 for the NAC and 0.11 for the WAC. These uncertainties are large compared to the difference (1.0 − CTE) we are trying to measure and so we retain the CTE measured before launch. Some

degradation to CTE has probably occurred during the mission but it is too small to detect in images up to mid-2009.

6. Photometric calibration

For photometric studies the measured data number (DN) values must be calibrated to yield photon intensities or fluxes, and for solar system objects the desired quantity is usually I/F where I is the reflected intensity and πF is the incident solar flux. After subtraction of bias and the dark values and removal of 2-Hz noise (see Porco et al., 2004), data numbers are converted to electrons by use of the gain constant. The cameras have four gain states, and the gains were calibrated on a relative scale from observations of the same target at different gain states. Electrons and photons are related by Eq. (2) from Porco et al. (2004):

$$e_p[i,j] = C(f_1,f_2)A\Omega t(i)\mathrm{FF}(i,j,f_1,f_2)\int I(i,j,\lambda)T_0(\lambda)T_1(\lambda)T_2(\lambda)QE(\lambda)d\lambda \quad (2)$$

In Eq. (2) $e_p[i,j]$ is the photo-emitted electron count at pixel location $[i,j]$, A is the area of the primary lens or mirror, Ω is the solid angle subtended by each pixel, FF is the flat field response, f_1 and f_2 are filters in wheels 1 and 2, respectively, λ is the wavelength, and T_0, T_1 and T_2 are transmission functions of the optics and filters in wheels 1 and 2, respectively. These were measured in the laboratory.

After the shutter closes the potential wells are clocked down the line direction as the CCD is read out. The shutter blades move along the sample direction. The shutter blades accelerate and decelerate and so the exposure time $t(i)$ can depend on sample number. This dependence was measured before launch. We use the ground calibration for non-uniformity of the shutter, but we have updated the shutter offset (a constant term to be subtracted from the tabulated shutter time) using in-flight data. Our shortest exposure time is nominally 5 ms, but the shutter offset we derived for the NAC is almost half of that value. The constant exposure offsets calculated during ground calibration were 1 ms for the NAC and less than 0.5 ms for the WAC. From Vega analysis, we derived a NAC offset to be 2.85 ms. We used images showing azimuthal scans along Saturnian rings to determine the WAC offset to about 1.8 ms. Uncertainty on shutter offset is ± 0.25 ms.

Filter transmission curves are thought to be accurate to about 1% over most of the bandpass within 1% of the peak value. Transmission measurements were made out to several hundred nanometers from the central peak but accuracy of those measurements drops to a factor of 2 or worse once the transmission drops below about 10^{-3}. The purpose of in-flight photometric calibration is to determine the best values for the quantum efficiency of the detector, QE(λ) (electrons/photon), and the filter-dependent correction factors $C(f_1,f_2)$. If the component calibrations done prior to launch are accurate and if there are no changes during flight, then there should be no adjustment to pre-flight QE and the correction factors should be very close to 1.0.

Quantum efficiency is the most difficult quantity to measure for the camera system, it is associated with the greatest uncertainty, and so we first modify QE(λ) to achieve a better calibration. Adjustment to QE can affect more than one filter, so the correction terms $C(f_1,f_2)$ are used to make further corrections to individual filter combinations.

Use of Eq. (2) allows us to account fully for the shape of the filter and optics transmission functions which should be accurately known from laboratory measurement, and to use a variety of sources which have structure in their spectral content. This functionality is built into the CISSCAL, which has an option for an intensity or flux spectrum supplied by the user. We calculate the expected electron count by integrating all terms in Eq. (2). We compare the expected count with the observed count and modify the QE or the correction factors based on the difference until a weighted best fit is achieved.

All images used in this analysis were calibrated using version 3.4 of the CISSCAL calibration software. Default settings were used for all calibration steps with the exception of bias subtraction, for which we used the bias strip mean to estimate bias level, and 2-Hz noise removal, which we performed using a horizontally averaged "image mean" to approximate the 2-Hz noise level. Additional cosmic ray removal was also performed using a median box filter method, excluding the photometry aperture region surrounding each star target.

Spectrophotometric calibration targets are listed in Table 2. We selected several sources with different spectral characteristics to provide checks. Our primary stellar reference is the 115–2600 nm Vega spectrum from Bohlin and Gilliland (2004). Vega is an A0 spectral type star, with flux mostly increasing toward the blue until the Balmer discontinuity is reached at 364.6 nm. In principle the use of Eq. (2) should accommodate a spectral discontinuity but we were not able to fit all sources as accurately as desired and we suspect that the discontinuity is playing a role. We therefore added observations of fourteen hotter stars (spectral types O and B) which have reduced or no Balmer discontinuity. These are listed in Table 2. Vega images often required short (less than 50 ms) exposure times in broadband filters. Exposures less than 50 ms are most sensitive to errors in shutter offset and also to small variations in exposure time across the image or from one exposure to the next. To minimize shutter uncertainties, this analysis employed the in-flight values and used only images with exposure times greater than 40 ms.

For O- and B-type stars we used spectrophotometry reported in the VizieR catalog (Ochsenbein et al., 2000; Alekseeva et al., 1997). Spectra from that source extend from 320 to 800 nm. At shorter and longer wavelengths we extrapolated the flux as follows. First, we fit a Planck function to the catalog data to estimate surface temperature. We then selected a stellar model flux model from the Kurucz (1993) catalog (http://www.stsci.edu/hst/observatory/cdbs/k93models.html) corresponding to the estimated temperature and assuming solar metallicity and $g=10^5$ cm s^{-2}. We scaled the model spectra to the observed spectra at both ends (typically below 320 nm and above 800 nm), and then smoothed by 5 nm.

We also observed a G-type star HR 996 as an additional target to help minimize the effects of spectral shape when I/F is computed. HR 996 is fainter than Vega, so longer exposures could be used in broadband filters, reducing errors from shutter time variations. An even redder star (77 Tau, spectral type K0IIIb) was also observed. The star is a double, with 78 Tau (spectral type A7III) present in the image.

Enceladus data were used for relative (color) calibration. Over the range of wavelengths to which the ISS cameras are sensitive, solar system objects have a red spectrum. If we could image the Sun the calibration to I/F would be insensitive to the instrumental details. The geometric albedo of Enceladus is relatively flat in the visible with diminishing reflectivity at UV and near-IR wavelengths. We use an Enceladus spectrum from the STIS instrument on the Hubble Space Telescope (HST) provided by K. Noll (2008, private communication). Enceladus data also gave the best signal/noise ratio because star images cover only a few pixels.

Enceladus images were chosen for this analysis based on the following criteria:

- All images are unsummed and with 12-bit encoding.
- The sub-spacecraft phase angle is less than 30°.

Table 2
Celestial photometric targets.

Identifier	Alternate ID(s)	Spectral type	V Mag.	Flux references
Vega	α Lyr	A0V	0.3	Bohlin and Gilliland (2004)
Enceladus				Keith Noll (private communication, 2008)
HR 996	K Cet	G5Vv (solar analog)	4.83	Glushneva et al. (1998b) for 322.5–762.5 nm; Santos et al. (2001) for near-IR (normalized to Glushneva et al. spectrum); Heck et al. (1984) from IUE for 115.3–320.1 nm
77 Tau	HD 28307	K0IIIb	3.847	Bruzual–Persson–Gunn–Stryker catalog (Gunn and Stryker, 1983); located online at the Hubble Space Telescope compilation of astronomical catalogs
78 Tau		A7III	3.409	Burnashev (1985): 320–817 nm; Glushneva et al. (1998a): 322.5–762.5 nm; Kharitonov et al. (1988): 322.5–757.5 nm; Glushneva et al. (1998b): 597.5–1082.5 nm (normalized to average of previous three); Jamar et al. (1976): 136–254 nm; Heck et al. (1984) IUE: 115.3–320.1 nm
HR6527,	λ Sco,	B2IV	1.62	All spectra longward of 320 nm were taken from the Pulkovo Spectrophotometric catalog (Alekseeva et al., 1997) with the exception of HR1903, taken from the Southern Spectrophotometric Standards catalog (Hamuy et al., 1992, 1994, Vizier designation II/179); UV portion of spectra derived from Kurucz, 1993 model and scaled to match observed data
HR5191,	η UMa	B3V	1.852	
HR1713,	β Ori	B8Iab	012	
HR1790,	γ Ori	B2III	1.64	
HR1948,	ζ Ori	O9Iab	1.7	
HR2004,	κ Ori	B0Iab	2.049	
HR3165,	ζ Pup	O5Ia	2.210	
HR472,	α Eri	B3Ve	0.50	
HR6175,	ζ Oph	O9V	2.578	
HR2294,	β CMa	B1II	1.97	
HR2491,	α CMa	A1V	−1.47	
HR2618,	ε CMa	B2Iab	1.513	
HR5267,	β Cen	B1III	0.60	
HR1903	ε Ori	B0Iab	1.70	

Table 3
Image parameters for Enceladus calibration (average for each set).

Observation name	Number of images	Target pixel scale (km/pixel)	Phase angle (deg.)	Sub-spacecraft latitude	Sub-spacecraft longitude
ISS_048EN_GLOCOLA101_PRIME	25	2.92	26.0	−0.3	87.9
ISS_051EN_094W014PH001_PRIME	5	8.88	13.7	0.3	94.1
ISS_051EN_094W019PH001_PRIME	5	11.66	19.4	1.1	93.1
ISS_003EN_GEOLOG002_PRIME	3	1.14	23.4	−0.9	205.5
ISS_003EN_GEOLOG003_PRIME	3	1.07	22.3	−0.9	216.3
ISS_020EN_GEOLOG004_PRIME	22	0.91	29.4	−0.1	241.1
ISS_047EN_GLOCOL001_PRIME	5	1.78	15.0	−2.2	197.5
ISS_048EN_238W012PH001_PRIME	5	8.45	11.9	0.0	239.4
ISS_051EN_GLOCOLB101_PRIME	9	5.49	22.4	−0.8	226.8
ISS_051EN_238W023PH001_PRIME	4	5.82	23.1	−0.7	239.0

- The target distance is greater than 100,000 km such that entire satellite fits within the field of view, and subtends at least 100 pixels in diameter.
- There are no corrupted data or missing lines near the target.
- We excluded all data outside a narrow range in geometry (sub-spacecraft latitude $<10^{\circ}$, sub-spacecraft longitude $<250^{\circ}$) to minimize variations intrinsic to the surface of Enceladus.

Enceladus images used in this analysis were taken with the anti-blooming camera bit set to ON. This imaging mode has been seen to cause excess noise in long-exposure images. We sought to minimize the excess noise problem by excluding images with a high noise level. For images with exposures longer than 1 s and fewer than 50,000 pixels on Enceladus, we measured the standard deviation of a 1×600 pixel horizontal strip centrally located 100 pixels from the bottom of the image. If the standard deviation exceeded 10% of the mean value the image was discarded. A synopsis of images used in this analysis, with their associated camera and geometry parameters appears in Table 3.

The absolute flux from Enceladus is a function of viewing geometry, and we were not able to reproduce the nearly directly back-scattering viewing geometry obtained for the HST observations. We assumed that color variation is a weak function of phase angle and that we could use low-phase ISS Enceladus images together with the HST spectra to apply color (filter A relative to filter B) constraints. K. Noll (private communication, 2008) observed both the leading and trailing Enceladus hemispheres with STIS, and reported identical results, within measurement error. This gave us some confidence that our use of Enceladus for color calibration would be insensitive to variations in sub-spacecraft latitude, but we still restricted our image set to minimize viewing geometry variations.

For the term $I(i,j,\lambda)$ in Eq. (2) we supplied the product of the geometric albedo spectrum from K. Noll and the solar flux (see Porco et al., 2004, Fig. 23). The solar flux is part of the CISSCAL

Table 4
NAC photometry standard deviations.

Filters	Images	σ_1	σ_2
UV1,CL2	14	0.096	0.109
UV2,CL2	29	0.064	0.065
UV2,UV3	9	0.118	0.120
CL1,UV3	18	0.059	0.059
CL1,BL2	49	0.040	0.052
BL1,CL2	6	0.034	0.052
BL1,GRN	39	0.059	0.085
CL1,GRN	12	0.020	0.021
RED,GRN	6	0.016	0.016
CL1,CL2	8	0.028	0.043
CL1,MT1	37	0.044	0.045
CL1,CB1	34	0.037	0.039
RED,CL2	4	0.024	0.024
HAL,CL2	35	0.038	0.038
RED,IR1	7	0.016	0.024
CL1,MT2	36	0.041	0.041
CL1,CB2	41	0.041	0.047
CL1,IR1	12	0.046	0.048
IR2,IR1	39	0.033	0.045
IR2,CL2	17	0.034	0.035
CL1,MT3	46	0.054	0.062
IR2,IR3	37	0.035	0.048
CL1,IR3	43	0.034	0.048
CL1,CB3	49	0.083	0.086
IR4,IR3	36	0.041	0.058
IR4,CL2	38	0.040	0.061

σ_1 is the standard deviation about the mean of the ratio of the measured photoelectron generation rate to the expectation value given by Eq. (2). σ_2 is the standard deviation of the ratio about the value of 1.0 (see Fig. 7).

support file package (solarflux.tab). Bias and 2-Hz noise removal were handled as follows: for images in which the target satellite subtends fewer than about 300 pixels in diameter, a dark-sky mask file was created (one for each observation), and used along with the "Image Mean" method of 2-Hz noise removal. For images in which the target satellite subtends greater than about 300 pixels in diameter, no mask file was created, and the overclocked pixel arrays were used for both 2-Hz noise and bias level removal. A cosmic ray removal algorithm was applied to all images, and then photometry performed in a straightforward manner: by summing the total I/F and then dividing by the total number of pixels on the target, $n_{pix}=\pi(r_{sat}/\text{pixscale})^2$, where r_{sat} is the satellite radius and pixscale is the target pixel scale in km/pixel. This step accounted for the $(1/\text{distance})^2$ dependence of the flux.

Two additional corrections were applied to the Enceladus photometry data. First, a phase angle correction using an Enceladus phase curve model (unpublished work by P. Helfenstein), and second, a "lost light" correction to recover any light from the extended tail of the point spread function that has fallen outside the frame. To do this, we created a synthetic image of Enceladus subtending the same number of pixels as the source image, and then convolved it with the PSF for that filter. Then we could simply calculate the fraction of the resultant flux falling outside of the camera's field of view, and add this back to the original image before summing. The PSF correction made less than a 0.6% total flux difference for all images except for a single UV1, CL2 image, for which it added 1.61%.

Measurement uncertainties were estimated from the standard deviations of individual measurements of stars. These are listed in Table 4 for the NAC and Table 5 for the WAC. Additional uncertainty in the absolute calibration derives from uncertainty reported in the literature for Vega (Bohlin and Gilliland, 2004).

The results of these steps are shown in Figs. 7–11.

Table 5
WAC photometry standard deviations.

Filters	Images	σ_1	σ_2
CL1,VIO	31	0.025	0.062
CL1,BL1	70	0.043	0.066
CL1,GRN	30	0.074	0.083
CL1,CL2	58	0.066	0.078
CL1,RED	71	0.065	0.079
CL1,HAL	41	0.046	0.064
MT2,CL2	51	0.027	0.053
CL1,IR1	3	0.019	0.027
CB2,CL2	76	0.032	0.036
IR2,IR1	85	0.020	0.029
IR2,CL2	82	0.036	0.061
MT3,CL2	48	0.051	0.059
IR3,CL2	62	0.050	0.050
CB3,CL2	38	0.027	0.031
IR4,CL2	40	0.028	0.033
IR5,CL2	22	0.023	0.023

Parameters have the same meaning as in Table 4

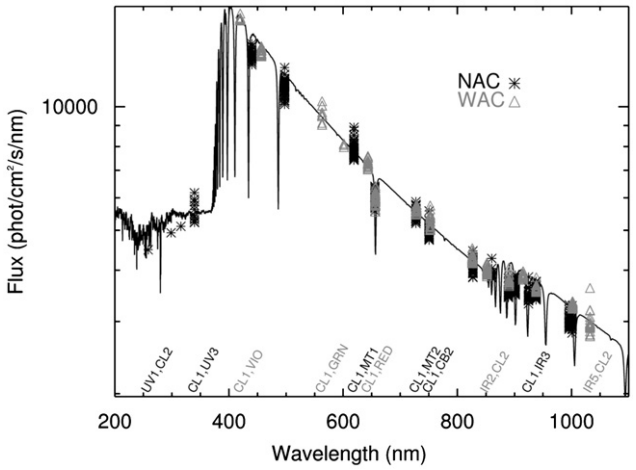

Fig. 7. Measured flux from Vega from ISS (symbols) and from Bohlin and Gilliland (2004). Wavelengths for the symbols in this figure and for other stars are effective wavelengths calculated by convolving the filter transmission with the input spectrum. They differ slightly from the central effective wavelengths. Several of the filter combinations are labeled near the bottom of the plot (NAC filters in black, WAC filters in a lighter shade).

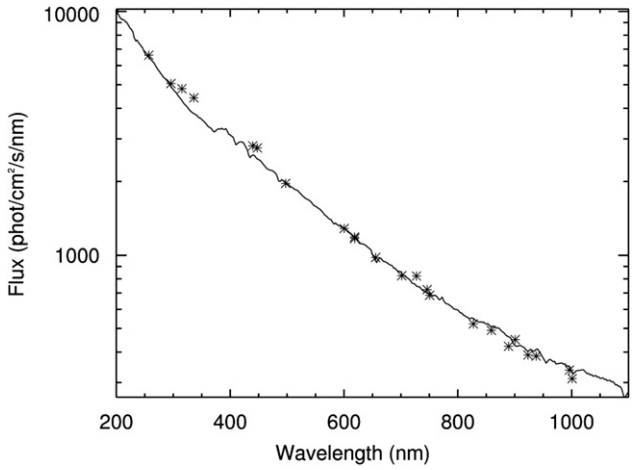

Fig. 8. NAC photometrically calibrated results for HR 2294 (β CMa). Symbols are ISS measurements. The solid curve longward of 320 nm is from the Pulkovo Spectrophotometric catalog (Alekseeva et al., 1997). At shorter wavelengths it was extrapolated as described in the text.

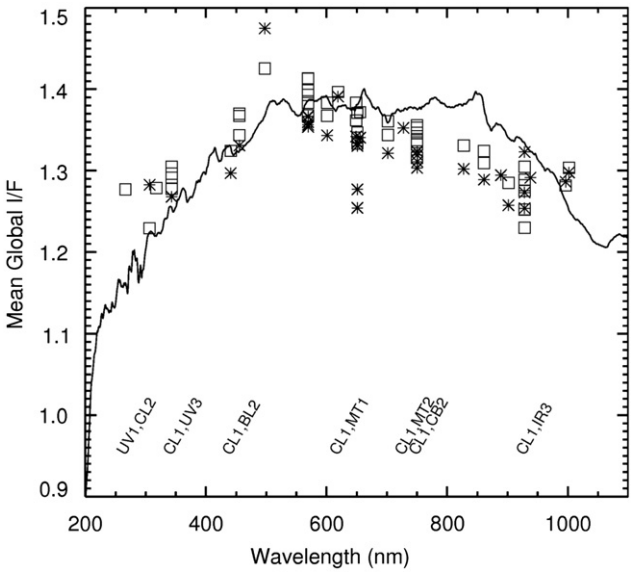

Fig. 9. Average whole disk relative reflectivity of Enceladus from Noll (private communication, 2008) and from NAC images (symbols). Asterisks are for the leading hemisphere and squares are for the trailing hemisphere. The ISS values were normalized by integrating the Noll spectrum over system transmission for each filter combination to obtain reference I/F values, and then scaling to the average I/F offset for all filters. Central wavelength locations for some of the filter pairs are indicated.

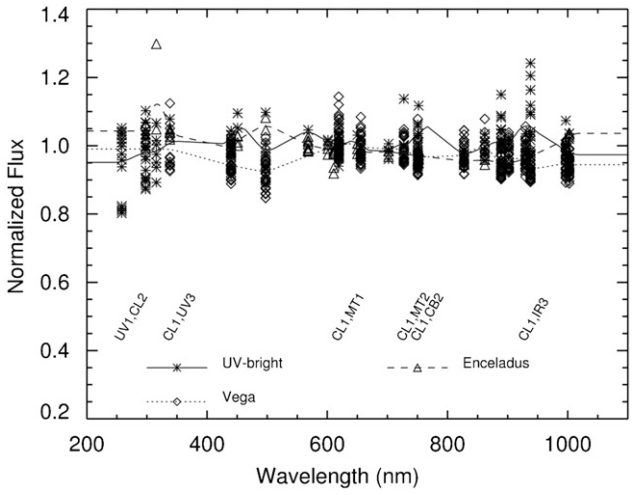

Fig. 10. NAC photometric results for Vega, Enceladus and a collection of UV-bright stars listed in Table 2 are shown together by plotting the ratio of the observed photoelectron production rate by the rate calculated from Eq. (2) using our derived calibration values. Enceladus values have been normalized to the average offset from Vega. The central wavelengths for some of the filter combinations are indicated.

7. Red leak

The term "red leak" is generally used to describe transmission of light at wavelengths far from the central wavelength of a filter. This non-ideal behavior is mostly a concern for ultraviolet filters because the reflected solar flux is generally much higher at long wavelengths relative to short wavelengths. With the dual filter wheels on the ISS cameras we could assess the blocking ability of the UV filters at long wavelengths. Filter transmission measurements were made prior to launch. At wavelengths far from the central wavelength the measured transmission was typically near the limit of sensitivity of the laboratory spectrophotometer

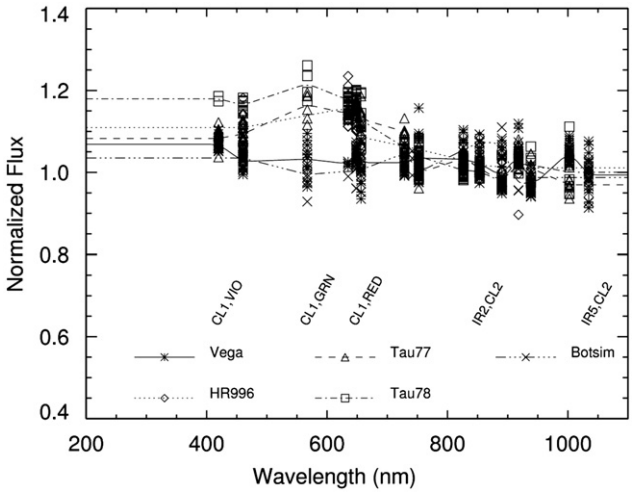

Fig. 11. Photometric results for Vega and three red stars imaged by the WAC are shown together by plotting the ratio of the observed photoelectron rate divided by the rate calculated from Eq. (2) using our derived calibration values. In addition we show corrections from BOTSIM images of Saturn where the requirement is to produce the same value of I/F in both cameras. BOTSIM and red star data has been normalized to Vega at wavelengths >700 nm.

($\sim 10^{-7}$–10^{-8}). Our first task was to check these against observed values in long exposures of Vega. To do this we made use of Eq. (2). The results of this calculation and the observed electron rates are shown in Table 6. In most cases a signal was not detected. In a few cases where the signal was detected the observed electron production rate was within about 25% of the rate predicted by Eq. (2), consistent with the laboratory measurements and their uncertainties, and with uncertainties in the stellar flux measured from the images.

8. Polarimetric calibration

Calibration of the linearly polarizing filters requires additional steps because separate images for each polarizer must be combined to form I, P and ϑ, or I and Q depending on whether three NAC or two WAC polarizers are used. In the previous sentence I is the intensity, P is the degree of linear polarization (0–1.0 or 0–100%), ϑ is the angle the electric vector that the polarized component makes with the camera Y-axis (closely aligned with the spacecraft Z-axis; see Porco et al. (2004) for a discussion of the camera coordinate system), and Q is the Stokes Q component of polarization (Stokes, 1860; Hansen and Travis, 1974), also defined with respect to the camera Y-axis. In the NAC the visible polarizers (which are effective from about 350 to 750 nm) are mounted so that they transmit primarily light whose electric vector makes angle ζ with respect to the camera Y-axis, where ζ is close to 0° (filter $P0$), 60° ($P60$) and 120° ($P120$). In the WAC there are two near-infrared polarizers at 0° (IRP0) and 90° (IRP90). The NAC also has an IRP0 filter.

The amount of light transmitted through the polarizers depends on the state of the incident light and on the transmission values of the parallel and perpendicular components (T_1 and T_2). Both transmission values vary with wavelength. The calibration procedure uses effective transmissions for each component averaged over the bandpasses of the paired filters. Eq. (3) expresses the transmission of light through the polarizers and is the starting point for derivation of the calibration procedure

$$I_0 = \tfrac{1}{2} I_u (T_1 + T_2) + I_p \left[\cos^2(\vartheta) T_1 + \sin^2(\vartheta) T_2 \right] \quad (3)$$

Table 6
Red leak results for NAC UV filters.

Filter Combination	Expected photons ($cm^{-2}\,s^{-1}$)	Measured photons ($cm^{-2}\,s^{-1}$)	Ratio	UV-filter transmission at peak wavelength of long-wave filter	Long-wave filter transmission at peak wavelength of UV filter
UV1,CB2	0.010	No detection		2.2×10^{-7}	$<1\times10^{-7}$
UV2,CB2	0.012	No detection		1.8×10^{-7}	$<1\times10^{-7}$
UV2,CB1	0.023	No detection		3.4×10^{-7}	$<1\times10^{-7}$
HAL,UV3	0.024	No detection		2.7×10^{-7}	$<1\times10^{-7}$
UV1,CB1	0.036	No detection		2.0×10^{-7}	$<1\times10^{-7}$
UV1,BL2	0.061	No detection		1.4×10^{-7}	1.3×10^{-7}
UV2,IR3	0.084	No detection		4.1×10^{-7}	[c]
UV1,IR3	0.096	No detection		2.9×10^{-7}	[c]
UV1,IR1	0.11	0.033[a]	0.30	$<1\times10^{-7}$	$<1\times10^{-7}$
UV2,IR1	0.13	No detection		$<1\times10^{-7}$	$<1\times10^{-7}$
UV2,BL2	0.15	0.16[b]	1.1	2.2×10^{-7}	$<1\times10^{-7}$
UV2,GRN	0.21	No detection		2.7×10^{-7}	1.5×10^{-7}
RED,UV3	0.24	No detection		3.5×10^{-7}	1.3×10^{-7}
UV1,GRN	0.26	No detection		2.1×10^{-7}	$<1\times10^{-7}$
IR4,UV3	0.27	0.22	0.79	8.8×10^{-7}	2.0×10^{-7}
IR2,UV3	1.1	0.87	0.77	6.3×10^{-6}	$<1\times10^{-7}$
BL1,UV3	4.0	3.6	0.89	1.9×10^{-7}	$<1\times10^{-7}$

[a] Very rough estimate, barely above noise.
[b] Contaminated by cosmic rays.
[c] We do not have a record of spectrophotometer measurements for IR3 at wavelengths shorter than 661 nm.

where I_0 is the intensity of light passing through the P_0 polarizer, I_u is the unpolarized component and I_p is the linearly polarized component of the intensity incident on the polarizer and ϑ is the angle the electric vector makes with the camera Y-axis. All angles are expressed in degrees with reference to the camera Y direction. Similar expressions for I_{60}, I_{90} snf I_{120} are obtained with ϑ replaced by $\vartheta-60$, $\vartheta-90$ and $\vartheta-120$.

These expressions can be solved to yield

$$I = I_u + I_p = \frac{2(I_0+I_{60}+I_{120})}{3(T_1+T_2)} \tag{4}$$

$$I_p^2 = \left[\frac{2(-2I_0+I_{60}+I_{120})}{3(T_1-T_2)}\right]^2 + \left[\frac{(I_{60}-I_{120})}{(T_1-T_2)\sin(120)}\right]^2 \tag{5}$$

$$\vartheta = \frac{1}{2}\mathrm{Arctan}\left\{\frac{3(I_{120}-I_{60})}{2\sin(120)(-2I_0+I_{60}+I_{120})}\right\} \tag{6}$$

For the infrared polarizers,

$$I = \frac{I_0+I_{90}}{T_1+T_2} \tag{7}$$

$$Q = \frac{I_{90}-I_0}{T_1-T_2} \tag{8}$$

The polarizing filters were mounted with small alignment errors, and so the angles are not exactly 0°, 60°, 120° and 90° and the resulting equations are more complicated. The angle offsets were measured as part of the ground calibration work and our polarization extraction software takes this into account. Angle offsets for the NAC are −0.5°, 1.8°, 0.8° and 2.3° for the P0, P60, P120 and IRP0 polarizers, respectively. Offsets for the WAC are 0.0° and 0.9° for IRP0 and IRP90. The angle is measured clockwise from the camera Y-axis, so an offset of 0.9° for the WAC IRP90 polarizer means that the principal axis of the polarizer is 90.9° from the camera Y-axis measured in the clockwise direction. The calibration constants for the polarizers in CISSCAL are tied to the calibration constants of the bandpass filters so that if a recalibration of the bandpass filter results in a change, the calibrated intensity with the polarizer (Eqs. (4) and (7)) will reflect that change. Calibration constants for the polarizers were determined by imaging icy satellites or Titan with the polarizers paired with each sensible bandpass filter. Images with clear filter paired with the same bandpass filter were also obtained, and the polarizer calibration constants were obtained by requiring that the intensity be equal in both sets of calibrated images. This exercise was performed on 3–6 targets for each sensible bandpass filter. Figs. 12 and 13 illustrate the results with images that were not part of the calibration.

Fig. 12. Images in the top half show the intensity of Titan at phase angle 106°. On the left is I/F from one NAC image (N1617163704) using the filter combination [CL1,BL2]. On the right is I/F derived from BL2 with three polarizers given by Eq. (4). In both cases the brightest pixels correspond to I/F=0.14. The bottom half of the image shows the degree of linear polarization (left side) and angle of polarization. The left image is scaled such that the brightest pixel corresponds to degree of polarization =75%. The angle of polarization is close to 0 (electric vector perpendicular to the sun direction) with maximum deviation about ±3.5° near the poles.

9. Point spread function

The point spread function (PSF) depends on the camera (WAC or NAC) and on the filter combination. Images to determine the

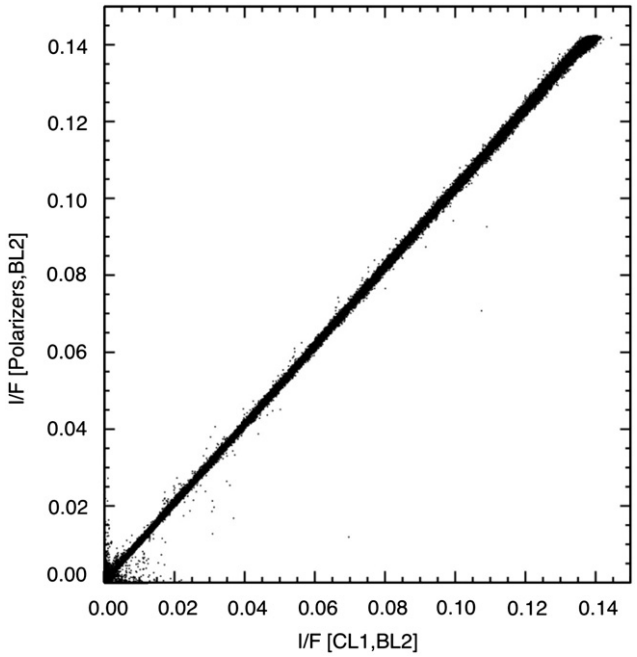

Fig. 13. *I*/*F* values of Titan in the BL2 filter from Fig. 12 are shown as a small dot for every pixel for the polarizer combination (using Eq. (4)) versus the clear filter CL1. The goal of the polarization calibration is to bring the *I*/*F* value using polarizers into agreement with the value using the CL1 filter.

PSF were obtained as part of the pre-flight calibration procedure. However, the dynamic range of the pre-flight calibration images was not great enough to measure the PSF out to the edges of the detector. The PSF might also be influenced by events that occurred after launch. Porco et al. (2004) described a contamination event which occurred after the Jupiter flyby in 2000. The event grossly changed the nature of the PSF for the NAC. After the contamination event the NAC was kept at an elevated temperature for many hours to reduce the contaminant. That operation was successful but it is possible that some residual contaminant remains, requiring a measurement of the PSF.

In-flight measurements of the PSF were made from short exposures of bright stars. There are not enough star images to derive the PSF as a function of location in the image, so one PSF was assembled from a composite of several images. Multiple images were combined for two purposes. First, the dynamic range of the CCD is less than what is needed to measure, in unsaturated exposures, the PSF from the center of the star image out to several hundred pixels from the center. Second, the PSF is unresolved by the pixel and so multiple images with small offsets were combined to derive the shape of the PSF at sub-pixel resolution. To cope with the dynamic range problem we combined multiple exposures including saturated images. Unsaturated images provided a high signal/noise measure of the PSF from its peak value to about 0.03 of peak value. To go beyond that range we used images which were saturated at the core of the star image but unsaturated further out. By splicing together the unsaturated parts of deeper exposures we were able to extend the PSF dynamic range to 10^4 for most filters.

To get even greater dynamic range we used satellite images with target diameter in the range from a few tens of pixels to about two hundred pixels. Although these are not point sources (and therefore the central part of the PSF cannot be derived from them) the PSF at large distance (beyond about 2 satellite radii) can be derived approximately because of the strong signal from a target occupying 100–10^4 pixels. By combining images of satellites having a variety of angular sizes we were able to produce a composite PSF which took advantage of the region in each image where the signal/noise was sufficient but yet not too close to the satellite limb. Compact targets (circular or nearly circular) work best for this procedure and so we selected images in the phase angle range less than 30° for the NAC and less than 45° for the WAC. The image set meeting these criteria for the WAC was smaller than that for the NAC, and we were not able to derive extended PSFs for many of the WAC filters.

The procedure was an iterative one. A trial extended PSF (one that extends all the way to the edge of the frame) was used to deconvolve a satellite image. A threshold was then established such that image values smaller than that threshold were set to zero. The threshold was chosen to be near the half-light point near the bright limb, and smaller values beyond the threshold were set to zero in accord with the idea that the background sky should be zero. Internal to the threshold boundary the image was thought to be from the satellite and the total was scaled to agree with the original total. This produced an approximation to a deconvolved image. Next the image was convolved with the trial PSF. A ratio of the resulting image to the data image provided a basis for improving the PSF, and the process was repeated. After three iterations the solution would converge and the values in the synthetic convolved image would agree with the data at large distance. This was done for each of several satellite images with different angular diameters, and a composite was constructed from the results. The four NAC or six WAC diffraction spikes from the secondary spider veins were not reproduced by this method because the satellite image was generally larger than the width of the diffraction spike. The diffraction spikes at large distance from the center were restored by extrapolating from the inner core. For this same reason the resulting PSF at large distance does not contain detail smaller than about 100 pixels except for the extrapolated diffraction spikes. A smoothing procedure was also applied to reduce noise, but only in the azimuthal direction since the detail in the radial direction is important to retain. Table 7 and 8 summarize the key findings of this effort. With these procedures we achieved a PSF with a dynamic range greater than 10^7.

A typical PSF is depicted in Fig. 14. That PSF is for the NAC [BL1,CL2] filter combination.

Table 7
NAC in-flight PSF results.

Filter Pair	Width at half-max (Pixels)	Dynamic range	Extended PSF? Default is "Yes"
BL1_CL2	1.33	1.3×10^8	Yes
BL1_GRN	1.27	1.1×10^7	Yes
CL1_BL2	1.25	9.0×10^7	Yes
CL1_CB1	1.34	2.9×10^3	No
CL1_CB2	1.39	7.7×10^7	Yes
CL1_CB3			Yes
CL1_CL2	1.29	9.0×10^7	Yes
CL1_GRN	1.42	8.8×10^7	Yes
CL1_IR1	1.44	7.1×10^7	Yes
CL1_IR3	1.45	6.2×10^7	Yes
CL1_MT1	1.24	9.8×10^7	Yes
CL1_MT2	1.34	8.3×10^7	Yes
CL1_UV3	1.45	7.8×10^7	Yes
HAL_CL2	1.25	9.0×10^7	Yes
IR2_CL2	1.56	5.9×10^7	Yes
IR2_IR1	1.34	7.8×10^7	Yes
IR2_IR3	1.39	6.7×10^7	Yes
IR4_CL2	1.53	6.1×10^7	Yes
IR4_IR3	1.40	6.5×10^7	Yes
RED_CL2	1.40	8.4×10^7	Yes
RED_GRN	1.31	9.2×10^7	Yes
RED_IR1	1.37	7.8×10^7	Yes
UV1_CL2	1.29	8.9×10^7	Yes
UV2_UV3	1.34	8.6×10^7	Yes

Table 8
WAC in-flight PSF results.

Filter pair	Width at half-max (Pixels)	Dynamic range	Extended PSF? Default is "Yes"
CB2_CL2	1.38	3.6×10^{7}	No
CB3_CL2	1.77	2.1×10^{7}	No
CL1_BL1	1.46	2.2×10^{7}	Yes
CL1_CL2	1.72	1.8×10^{7}	Yes
CL1_GRN	1.19	4.9×10^{7}	Yes
CL1_HAL	1.08	1.4×10^{8}	No
CL1_IR1	1.57	4.3×10^{7}	Yes
CL1_RED	1.41	3.4×10^{7}	Yes
CL1_VIO	1.12	2.1×10^{7}	Yes
IR2_CL2	1.61	6.3×10^{7}	No
IR2_IR1	4.67	3.1×10^{6}	No
IR3_CL2	1.49	2.6×10^{7}	Yes
IR4_CL2	1.48	3.7×10^{7}	No
IR5_CL2	1.37	4.7×10^{7}	No
MT2_CL2	1.34	1.5×10^{8}	No
MT3_CL2	1.64	3.6×10^{7}	No

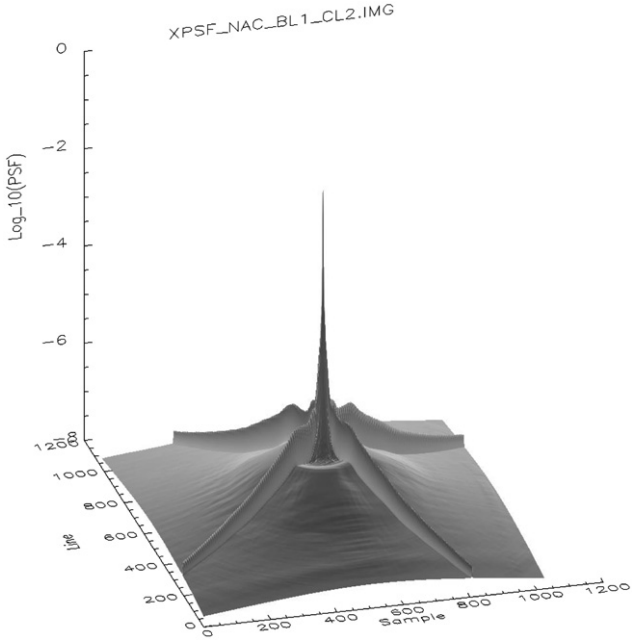

Fig. 14. A typical PSF for the NAC (rendered on a base-10 logarithmic scale), in this case for filter pair [BL1,CL2]. The vertical axis is the base-10 logarithm of the PSF.

Fig. 12. The images in the top half show the intensity of Titan at phase angle 106°. On the left is I/F from one NAC image (N1617163704) using the filter combination [CL1,BL2]. On the right is I/F derived from BL2 with three polarizers given by Eq. (4). In both cases the brightest pixels correspond to $I/F=0.14$. The bottom half of the image shows the degree of linear polarization (left side) and angle of polarization. The left image is scaled such that the brightest pixel corresponds to degree of polarization $=75\%$. The angle of polarization is close to 0 (electric vector perpendicular to the sun direction) with maximum deviation about $\pm3.5^{\circ}$ near the poles.

The NAC Green filter PSF exhibits a subsidiary peak (a ghost image) as shown in Fig. 15.

The subsidiary peak is seen in combination with BL1 and also with the clear filter in the first filter wheel. It is probably due to an internal reflection. We do not understand why this would be the case only for the Green filter. More generally, internal reflections and stray light from the camera structure are probably responsible for the slow fall-off of the PSF at distances greater than a few

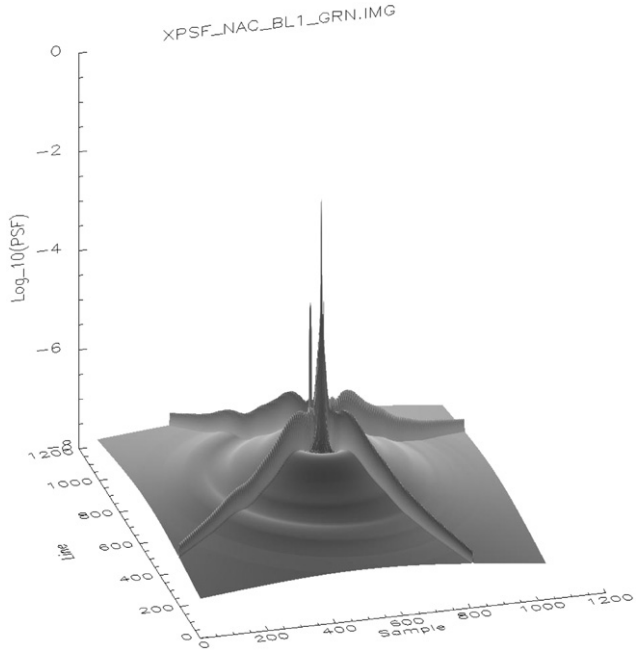

Fig. 15. An unusual PSF, for the NAC filter pair [BL1,GRN], which has a ghost feature a few tens of pixels away from the main peak and with an amplitude approximately 1% of the main peak. Such a feature is also seen in the [CL1,GRN] filter pair but not in other filter .

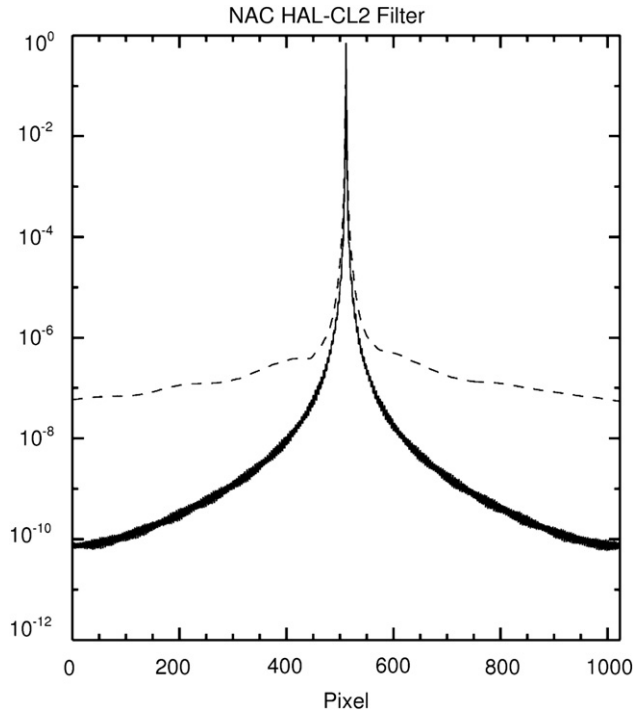

Fig. 16. Diametric profile across the horizontal direction of the NAC PSF for the narrow-band HAL-CL2 filter combination (dashed curve) and a theoretical PSF based on a diffraction calculation at the same mean wavelength.

pixels. Figs. 16 and 17 show how the measured PSF at red wavelengths compares to a PSF computed from the diffraction pattern of an annulus whose outer diameter is the diameter of the primary and whose inner diameter is that of the secondary mount (lamp holder in the case of the WAC). At large distance from the center the measured PSF is orders of magnitude larger than the diffraction-limited PSF. Heavily exposed images and images

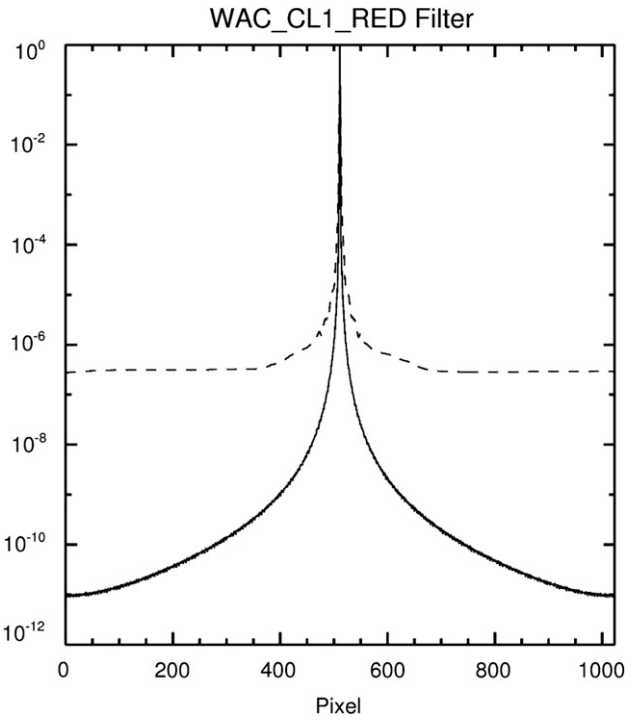

Fig. 17. Diametric profile across the horizontal direction of the WAC PSF for the CL1-RED filter combination (dashed curve) and a theoretical PSF based on a diffraction calculation at the same mean wavelength.

within 15–20° of the sun show stray light with complicated patterns. These patterns move and change depending on the apparent position of the light source. Our measured PSFs at large distances are a smoothed average using several images.

There is one other filter combination that exhibits anomalous properties. The WAC [IR2,IR1] combination has a PSF core that is significantly wider than all other WAC filter combinations (width at half maximum is almost five pixels). Because the WAC has a refractive objective it was not possible to bring all wavelengths to a common focus. The CL1 and CL2 filter thicknesses were individually optimized for best focus with the bandpass filters in the opposite wheel. The [IR2,IR1] combination is unable to take advantage of that optimization.

10. Stray light

Stray light is present when light is scattered onto the detectors by surfaces within or surrounding the cameras. Unlike the extended point spread function, the signal due to stray light depends not only on the pixel's distance from the source but also the orientation of the entire camera relative to the source. These artifacts are therefore very difficult to model, and we have not yet been able to develop a generic procedure for identifying or removing them. We will therefore simply review some properties of the stray light patterns we have identified in images taken during the Cassini Mission.

Some of the most prominent stray-light artifacts occur when relatively bright, compact sources (like moons or nearly edge-on rings) lie just outside the camera's field of view. These stray-light artifacts can possess a great deal of fine-scale structure that changes as the off-image object moves relative to the field of view. For the NAC, a bright object that lies just off the edge of the frame gives rise to bright streaks extending perpendicularly to the relevant edge, as well as more diffuse arc-like patterns

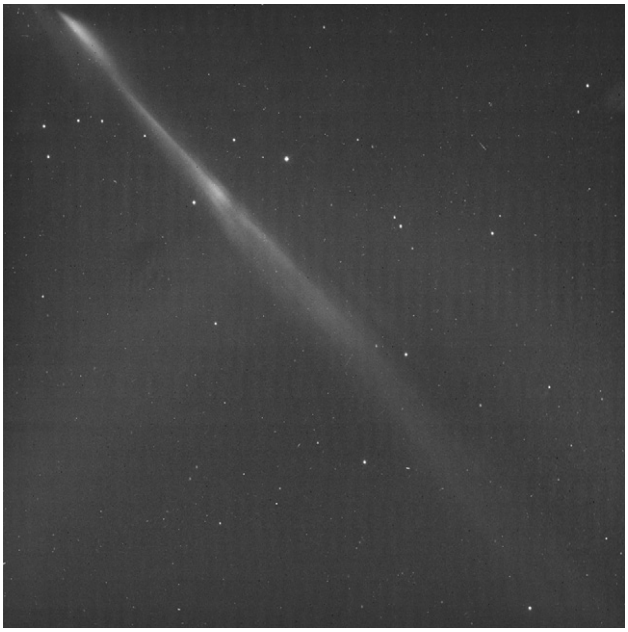

Fig. 18. Example of diagonal streak from stray light in a NAC image (N1472601232). This streak is produced by the satellite Tethys, which lies less than 1/2 of a NAC FOV off of the upper left corner of this image.

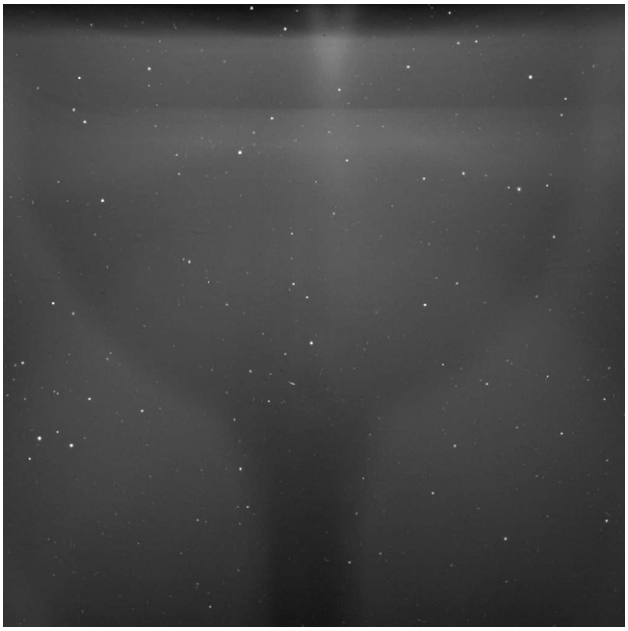

Fig. 19. Example of the diffuse patterns observed at moderate phase in the WAC. This image (W1486510390) shows the ansa of the E-ring at a vertically oriented bright feature near the top of the frame. The horizontal bands and the diffuse curving patterns extending over the image are attributed to stray light from the bright rings and planet that lie off the top edge of this image.

(c.f. Fig. 34A of Porco et al. 2004). Also, when a bright object is located near to the corners of the NAC frame, a bright streak can be seen to extend diagonally across the field of view (see Fig. 18). Similarly discrete features can be seen in some WAC images, along with more diffuse patterns that extend over the entire field of view (see Fig. 19). Some of the fine-scale structure in these artifacts becomes washed out when the apparent size of the off-axis sources is sufficiently large compared to the field of view, but there are also cases where stray light patterns persist in the

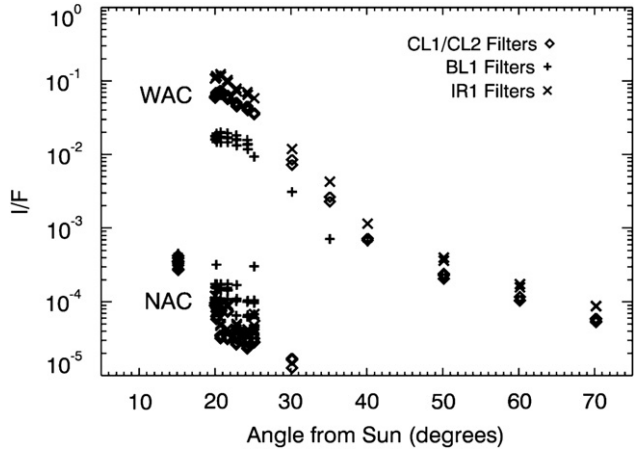

Fig. 20. The frame-average background sky brightness levels in the NAC and WAC as a function of angular separation from the Sun. This plot was made using a dedicated series of observations obtained on day 196 of 2002 and day 334 of 2003, during Cassini's cruise towards Saturn. The background sky brightness rises by several orders of magnitude between 70 and 20°, reaching an *I*/*F* level of nearly 0.1 in the WAC when the camera is pointed within 20° from the Sun (the WAC saturated at 15° from the sun), and the NAC pointed to within 15° of the sun. The sky brightness in the NAC is roughly three orders of magnitude lower than it is in the WAC.

images even when the source of the stray light is spatially extended. (For example, diagonal bands can be seen in close-up NAC images taken near the Saturn's bright limb.) The techniques required to remove these stray light patterns will therefore necessarily be highly context-dependent, but in many cases appropriate spatial filtering techniques should allow faint signals to be isolated from all but the worst of the artifacts.

In addition to the various structures visible within the images, stray light also contributes to the mean background signal in the images. Fig. 20 shows the measured background sky brightness in the cameras as a function of the cameras' orientation relative to the Sun, based on data from a specially designed imaging sequence obtained while the spacecraft was cruising towards Saturn. These data clearly show that the stray light levels in both cameras increase as the camera points closer to the sun, and that the stray light levels in the WAC are roughly three orders of magnitude higher than those of the NAC. In the WAC at least, the stray light levels seem to be somewhat higher in the infrared than the visible, which implies that the surfaces responsible for scattering the sunlight into the camera are more reflective at longer wavelengths. Other observations demonstrate that the brightness levels in both cameras depend not only on the angle of the camera axis relative to the sun, but also the azimuthal orientation of the camera (such variations are not apparent in Fig. 20 because these data come from a limited range of azimuthal angles).

We have not yet developed a complete model of the stray light brightness as a function of camera orientation and wavelength. However, as a practical matter the stray light levels in the NAC are sufficiently low that they do not seriously affect the ability of the camera to image faint objects. By contrast, the high backgrounds observed in the WAC (with background *I*/*F* values approaching 0.1 at 20° from the Sun) render it almost unusable for faint targets like diffuse rings or auroras at phase angles greater than 150° (unless the light from the sun is blocked from the camera by the Saturn).

11. Future work

New calibration images will be taken to fill gaps in the current calibration files (such as missing distant PSFs for some filters in Tables 7 and 8 and dust ring maps for the WAC). We plan to periodically update the hot pixel maps and the dust ring maps, and to check for changes in the photometric performance and charge transfer efficiency. Some of these, especially flat field images for the WAC, will require images close to Titan where the competition for spacecraft resources is intense, and it is not clear if a sufficient number of calibration images will be obtained. In addition, we continue to seek answers to the puzzles emerging from this effort. We would like to be able to account for the larger-than-expected variance of the stellar photometry. We would like to gain an understanding of what is responsible for the ghost image with the GRN filter and why it is not seen in other filters.

Acknowledgements

We are grateful to a number of people who have contributed to this work: Vance Haemmerle, Charles Avis, Philip Dumont, Jeff Cuzzi, S. Tom Elliott, Mike Evans, James Gerhard, Cynthia Kahn, Colin Mitchell, Keith Noll (who supplied the Enceladus spectrum), Kacie Shelton, and John Weiss. This research was carried out in part at the Jet Propulsion Laboratory, California Institute of Technology, under a contract with the National Aeronautics and Space Administration.

References

Alekseeva, G.A. Arkharov, A.A. Galkin, V.D. Hagen-Thorn, E.I., Nikanorova, I.N., Novikov, V.V., Novopashenny, V.B., Pakhomov, V.P., Ruban, E.V., Shchegolev, D.E. 1997. Pulkovo Spectrophotometric Catalog. VizieR Catalog: III/201.

Bohlin, R.C., Gilliland, R.L., 2004. Hubble space telescope absolute spectrophotometry of Vega from the far-ultraviolet to the infrared. Astron. J. 127, 3508–3515.

Burnashev, V.I. 1985. Catalogue of data on energy distribution in spectra of stars in a uniform spectrophotometric system, Abastumanskaya Astrofiz. Obs. Bull. 59, 83-90. VizieR catalog III/126.

Glushneva, I.N., Doroshenko, V.T., Fetisova, T.S., Khruzina, T.S., Kolotilov, E.A., Mossakovskaya, L.V., Shenavrin, V.I., Voloshina, I.B., Biryukov, V.V., Shenavrina, L.S. 1998a. Moscow Spectrophotometric Catalog of Stars. VizieR Catalog III/207.

Glushneva, I.N., Doroshenko, V.T., Fetisova, T.S., Khruzina, T.S., Kolotilov, E.A., Mossakovskaya, L.V., Ovchinnikov, S.L., Voloshina, I.B. 1998b. Sternberg Spectrophotometric Catalog. VizieR Catalog: III/208.

Gunn, J.E., Stryker, L.L., 1983. Stellar spectrophotometric atlas, wavelengths from 3130 to 10800 Å. Astrophys. J. Suppl. Ser. 52, 121–153.

Hamuy, M., Walker, A.R., Suntzeff, N.B., Gigoux, P., Heathcote, S.R., Phillips, M.M., 1992. Southern spectrophotometric standards. Astron. Soc. Pacific 104, 533–552.

Hamuy, M., Suntzeff, N.B., Heathcote, S.R., Walker, A.R., Gigoux, P., Phillips, M.M., 1994. Southern spectrophotometric standards. 2. Astron. Soc. Pacific 106, 566–589.

Hansen, J.E., Travis, L.D., 1974. Light-scattering in planetary atmospheres. Space Sci. Rev. 16, 527–610.

Heck, A., Egret, D., Jaschek, C., Battrick, B. 1984. IUE low dispersion spectra reference atlas. Part 1: normal stars. IUE low dispersion spectra reference atlas. Part 1: normal stars. ESA Special Publication: ESA SP-1052, ISSN 0379-6566.

Jamar, C., Macau-Hercot, D., Monfils, A., Thompson, G.I., Houziaux, L., Wilson, R. 1976. UV Bright Star Spectrophotometric Catalog. VizieR On-line Data Catalog: III/39A.

Kharitonov, A.V., Tereshchenko, V.M., Knyazeva, L.N., 1988. Spectrophotometric Catalogue of Stars. VizieR Catalog III/202. Alma-Ata, Nauka, p. 484.

Kurucz, R.L. 1993. Model Atmospheres. VizieR On-line Data Catalog: VI/39. Originally published in: 1979 Ap. J. Supp.

Ochsenbein, F., Bauer, P., Marcout, J., 2000. The VizieR database of astronomical catalogues. Astron. Astrophys. Suppl. 143, 23–32.

Porco, C.C., West, R.A., Squyres, S., McEwen, A., Thomas, P., Murray, C.D., DelGenio, A., Ingersoll, A.P., Johnson, T.V., Neukum, G., Veverka, J., Dones, L., Brahic, A., Burns, J.A., Haemmerle, V., Knowles, B., Dawson, D., Roatsch, T., Beurle, K., Owen, W., 2004. Cassini imaging science: instrument characteristics and anticipated scientific investigations at Saturn. Space Sci. Rev. 115, 363–497.

Santos, J.F.C., Jr., Alloin, D., Bica, E., Bonatto, C. 2001. Spectral Library of Galaxies, Clusters and Stars. VizieR On-line Data Catalog: III/219.

Stokes, G.G., 1860. On the intensity of the light reflected from or transmitted through a pile of plates. Proc. Roy. Soc. London 11, 545–557.